Effect of instrumental resolution and polydispersity on ideal form factor in Small Angle Neutron Scattering

Isabelle Grillo
Institut Laue Langevin, DS-LSS, 6 rue Jules Horowitz, B.P. 156, 38042 Grenoble Cedex 9
grillo@ill.fr

ILL Technical Report
ILL01GR08T

Abstract: The aim of Small Angle Neutron Scattering experiments is to extract the shape, distribution in size and structure of scatterers from data measured in reciprocal space. Ideal form factors models have been known for many years and have been further developed by many authors. The knowledge of the instrumental resolution is as important as the choice of the model. The finite divergence and size of direct beam, the wavelength resolution and the pixel size contribute to the smearing of the real intensity scattered by the sample. In this paper, the effects of the instrumental resolution and polydispersity of the scatterers are investigated and compared. Is the instrumental resolution a limitation for the structural characterization? The geometry of the spectrometer D22 (Institut Laue Langevin, Grenoble) will be taken as reference for the numerical and experimental applications but the equations are general and can be applied to others small angle neutron spectrometers. The calculations show that the effects of polydispersity or wavelength resolution are very similar, mainly smoothing of the form factor oscillations and broadening of Bragg peaks.

Synopsis: comparison between the effects of instrumental resolution and polydispersity of the scatterers in Small Angle Neutron Scattering data.

Introduction

The aim of Small Angle Neutron Scattering (SANS) experiments is to extract the shape, distribution in size and structure of scatterers from data measured in the reciprocal space. The term "scatterers" covers a large range of objects, like polymers, proteins, colloids, micelles, bilayers, aggregates, pores in solids…with typical sizes from 10 to 4000 Å. Ideal form factor models have been known for years; the spherical one was already calculated in 1911 by Lord Rayleigh (1911) and we can also named among the most used models: Guinier (1939) for ellipsoid, Debye (1947) for polymer chains, Fournet (1951) for cylinder, Teixeira (1988) for fractal. A very complete description of possible form factors is given in (Pedersen, 1997). However, in the most of the cases, these form factors do not represent the experimental data as well as expected. Instrumental resolution (Schmatz *et al.*, 1974), (Wignall *et al.*, 1988), (Mildner *et al.*, 1990), (Pedersen *et al.*, 1990) and polydispersity of the scatterers have to be introduced in the models. In this article, we propose first to investigate separately the two effects which will be compared in a last part. The experimental broadening of Bragg peaks illustrates the influence of the wavelength spread at large q.

In all the following, the consequences of polydispersity and resolution will be illustrated on the ideal form factor $F^2(q, r_0)$ of a spherical shell (Figure 1):

$$F(q,r_0) = \frac{3}{V_1 - V_0}\left[V_1 \frac{\sin(qr_1) - qr_1\cos(qr_1)}{(qr_1)^3} - V_0 \frac{\sin(qr_0) - qr_0\cos(qr_0)}{(qr_0)^3}\right] \qquad \textbf{(1)}$$

$$\text{with } r_1 = r_0 + e$$

q is the scattering vector ($q = 4p/l \sin q$); r_0 and r_1, the internal and external radii of the shell and V_0-V_1 its volume. We take r_0=200 Å and e=20 Å. We chose this example as the bumps and the sharp cusps are very sensitive to the resolution effects.

The geometry of the spectrometer D22 (ILL) has been taken as reference (D22 manual) for the numerical and experimental applications. The size of the collimation guide and the source is S=55x40 mm^2. In a standard experiment a 7x10 mm^2 aperture is placed in front of the sample to define the beam size at the ample position. The simulated curves are plotted between 10^{-3} to 0.5 $Å^{-1}$, a q-range that would be obtained with three sample to detector distances, D=18 m, 5.6 m and 1.4 m with λ=6 Å. We call collimation C is the distance between the end of the neutron guide and the sample. The size of the direct beam on the detector depends on the configuration, *i.e.* collimation and detector distance. By simple geometric consideration, one deduces the beam size on the detector: $S_d = S\,D/C$.

We consider only very dilute suspensions to neglect the structure factor (S(q)=1). The constant K_c, also called the contrast constant represents the product $(\Delta r)^2 \Phi (V_1 - V_0)$, Φ is the volume fraction

and $\Delta\rho$ the difference of length scattering densities between the shell and the environment. In these conditions, the ideal scattered intensity $I_{id}(q)$ is equal to:

$$I_{Id}(q) = K_C F^2(q, r_0) \quad \textbf{(2)}$$

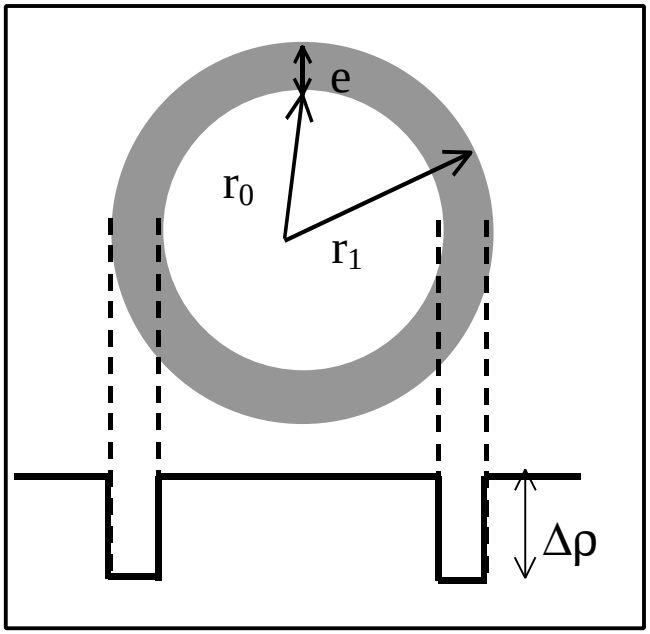

Figure 1: Parameters of the spherical shell used as model to illustrate the effect of resolution and polydispersity.

Instrumental resolution

The smearing of the ideal scattered intensity has three factors: the finite size of the incident beam, the wavelength resolution and the pixel size on the detector (Pedersen *et al.*, 1990). We consider here only the first two points since the pixel size (7.5x7.5 mm^2) has a negligible effect.

The q-resolution at a given q may be written according to a Taylor expansion as:

$$\Delta q = -q\left(\frac{dl}{l}\right) + \left(\frac{4p}{l}\right)\cos q\,\Delta q \quad \textbf{(3)}$$

Hence,

$$\Delta q^2 = q^2\left(\frac{dl}{l}\right)^2 + \left(\frac{4p}{l}\right)^2 \cos^2 q\,\Delta q^2 = \Delta q^2(l) + \Delta q^2(q) \quad \textbf{(4)}$$

$$= q^2\left[\left(\frac{1}{2\sqrt{2\ln 2}}\frac{\Delta l}{l}\right)^2\right] + \left[\left(\frac{4p}{l}\right)^2 - q^2\right]\Delta q^2$$

$\Delta\lambda/\lambda$ is related to the FWHM (full width at half maximum) value of the triangular function describing the wavelength distribution by FWHM=$\lambda_0(\Delta\lambda/\lambda)$. *Dq* is related the width of the direct beam (Figure 11). A detailed description of $\Delta\lambda/\lambda$ ($\delta\lambda/\lambda$) and *Dq* are given in the Appendix.

From (4), one sees clearly that Δq^2 depends on the wavelength spread and also on q. Taking λ=6 Å, $\Delta\lambda/\lambda$=10% and $\Delta\theta=2\times10^{-3}$ rad, typical values for a D22 experiment (see Table 1), the evolution of Dq^2 as a function of q is presented in Figure 2. The contribution from *Dq* is quasi-constant versus q. That from λ increases with q. At low q (< 10^{-2} Å^{-1}), the uncertainly on q is dominated by the distribution in angle. At large q-values, *Dq* is due to the wavelength spread.

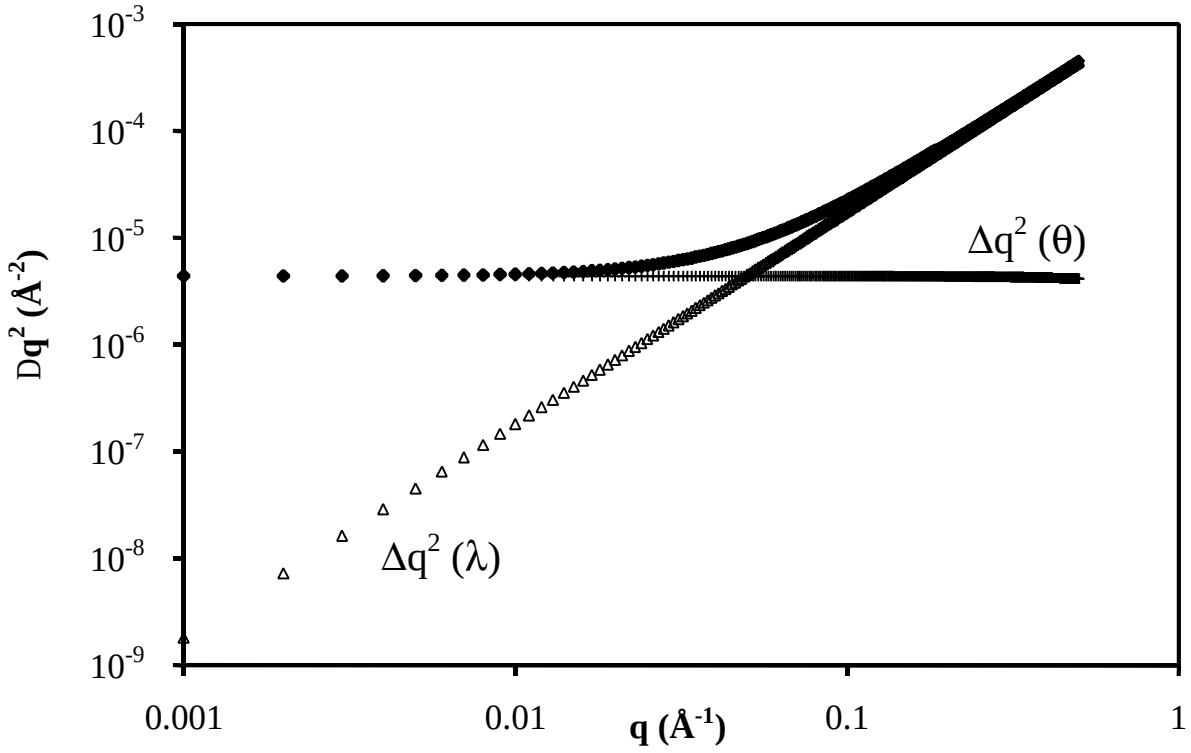

Figure 2: Contributions of Dl/l **(▲),** Dq **(+) to the total q-distribution,** Dq^2 **(◆). Curves are calculated for** l**=6 Å,** Dl/l**=10% and** Dq**=10^{-3} rad**.

The resolution function *R(q',q,Dq)* describes the distribution of the q-vectors at a given instrumental configuration. The experimental intensity I_{exp} is the real intensity scattered by the sample $K_cF^2(q,r_o)$ (2) smeared by the resolution function *R(q',q,Dq)*:

$$I_{\exp}(q) = \int_{q'-\infty}^{q'+\infty} K_c R(q', q, \Delta q) F^2(q, r_o) dq' \qquad \textbf{(5)}$$

Assuming a gaussian function for the resolution (Pedersen *et al*., 1990), equation 5 yields:

$$I_{\exp}(q) = \int_{q'\to-\infty}^{q'\to+\infty} K_c \frac{1}{\Delta q\sqrt{2p}} \exp\left(-\frac{(q'-q)^2}{2(\Delta q)^2}\right) F^2(q, r_o) dq' \qquad \textbf{(6)}$$

In practice, the range of integration *q'-8* , *q'+8* is replaced by *q'-a*, *q'+a* where *a* depends on the width of the gaussian function, *i.e.* on Dq^2. The higher Dq^2, the larger is the integration range which has to be used A too small integration range would yield to an underestimation of the smearing, particularly at high q. In Figure 3, the gaussian q-distribution at small and large q are shown. Dq^2 is

calculated assuming the same angle and wavelength distributions as in Figure 3, λ= 6 Å, $\Delta\lambda/\lambda$= 10% and $\Delta\theta$= 10^{-3} rad (*i.e.* $\Delta q(0)= 6x10^{-3}$ Å^{-1}). At small q, 5 points around q would be enough for the integration, whereas 30 points are needed at high q.

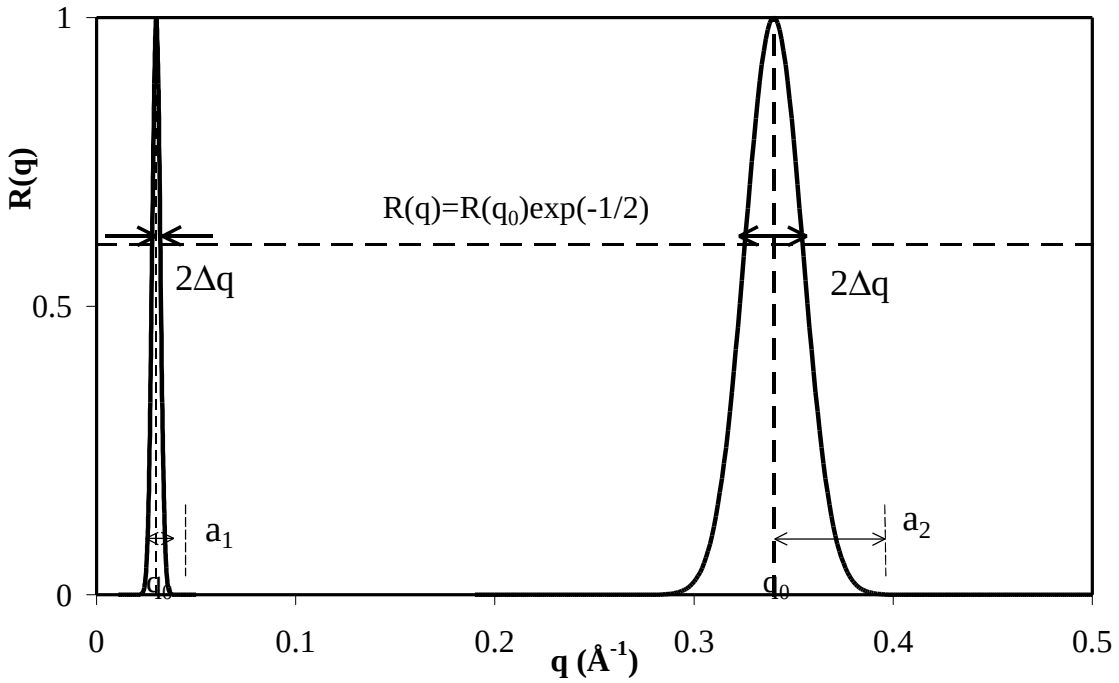

Figure 3: Gaussian q-distribution function and integration range at small and high q. l**=6 Å,** Dl/l**=10% and** Dq**=10^{-3} rad.**

Effect of the beam divergence and size: q resolution

As shown in Table 1 and Figure 11, *Dq* varies between $8x10^{-4}$ to $2.6x10^{-3}$ rad on D22. These smearing effects are presented in Figure 4. In insert, a zoom of the low-q region is presented; the direct beam size is compared to the width of the first oscillation of the ideal form factor and the resulting smeared curve is drawn. The direct beam size has a large influence at small angles inducing an intensity decrease of the plateau and smoothing the first oscillations.

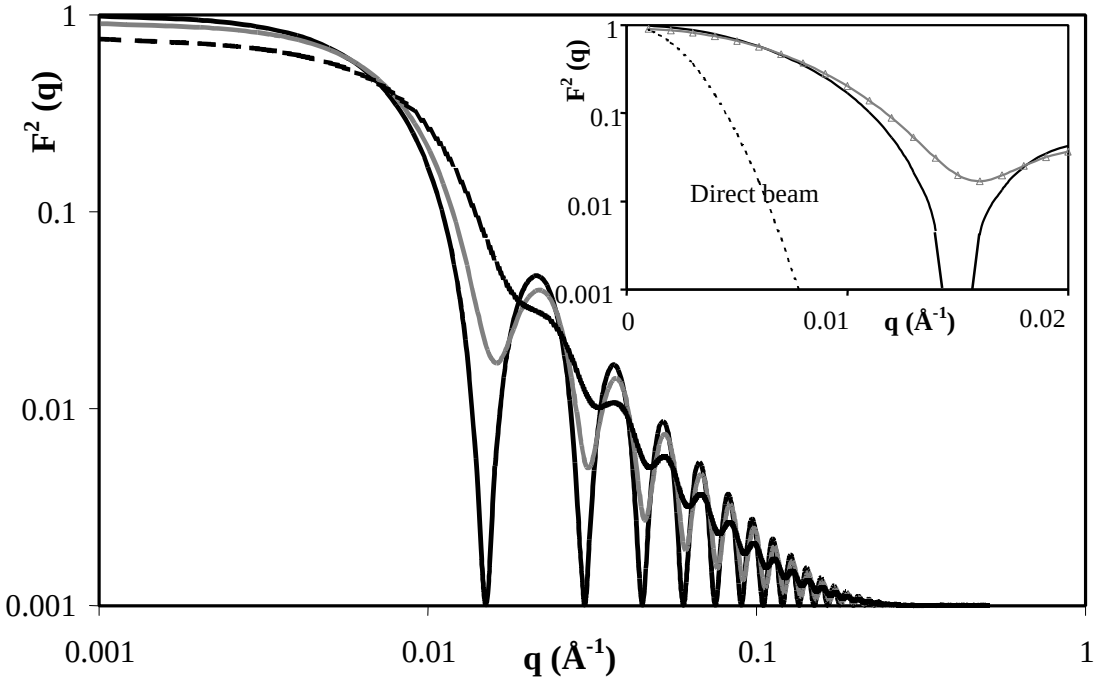

Figure 4: Effect of the Dq **on the ideal scattering of a monodisperse spherical shell, r_0=200 Å.** l**=6 Å and** Dl/l**=0. (▬) Dq=0 rad; (▬) Dq=1 10^{-3} rad corresponding to Dq(0)=2.1x10^{-3} Å-1; (▪▪▪▪) Dq=2x10^{-3} rad corresponding to Dq(0)=4.2x10^{-3} Å^{-1}**

Insert: comparison of the direct beam width (▪▪▪▪) Dq=1x10^{-3} rad (Dq(0)=2.1x10^{-3} Å^{-1}) with the width of the first oscillation of the form factor, (▬) Dq=0 and the resulting smeared curve (△) Dq=1x10^{-3} rad. Curves plotted in semi-log scale.

Effect of the l distribution

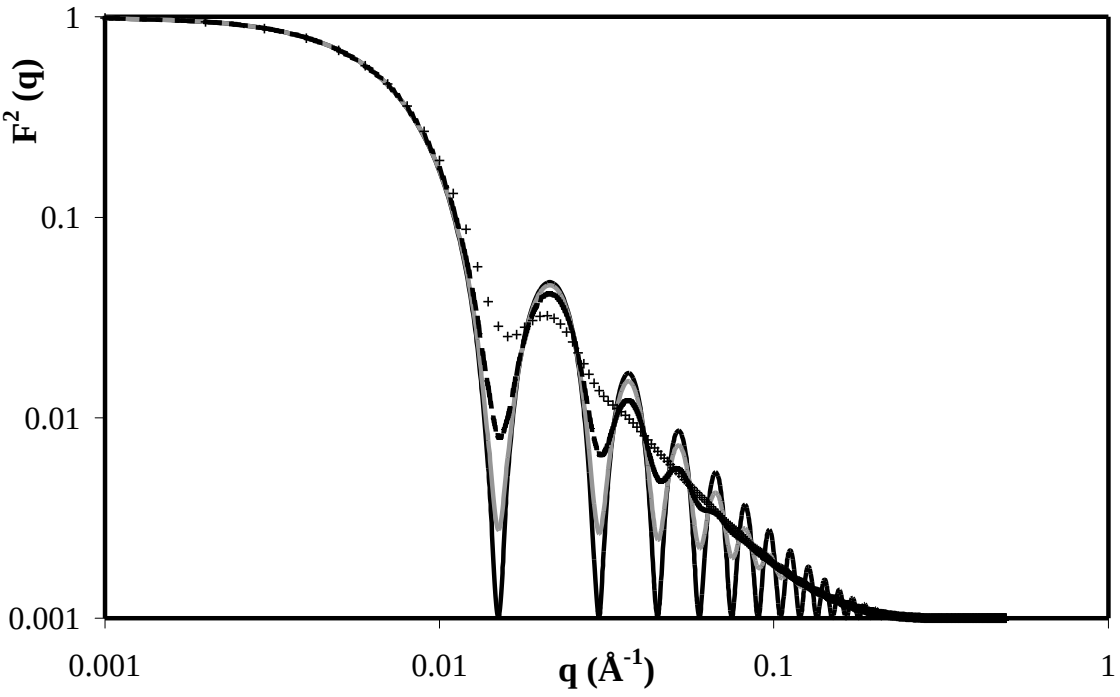

Figure 5: Effect of the wavelength resolution on the ideal scattering of a monodisperse spherical shell, r_0=200 Å. l**=6 Å and** Dq**=0. (▬) Dl/l=0; (▬)Dl/l=10%; (▪▪▪▪) Dl/l=20% and (+) Dl/l=40%.**

In Figure 5, one sees that on such a sample, the effects are most noticeable for $\Delta\lambda/\lambda>20\%$. Above this value, the oscillations vanish. Below 20%, the oscillations are still visible but a broadening is observed. In contrast with the θ-resolution, the smearing effects by λ are important at large q.

Application: Evidence of wavelength spread

A simple and easy experiment to demonstrate the wavelength spread is to use a polycrystalline sample, giving narrow Bragg peaks, with several orders at large angles (> 0.1 $Å^{-1}$). For example tetradecanol, octadenol (Né *et al.*, 2000) or silver behenate (Huang *et al.*, 1993) are currently used for q-range calibration and give their first order Bragg peak at q_b : 0.1583, 0.1521 and 0.10763 $Å^{-1}$ respectively.

In this range of q larger than 0.1 $Å^{-1}$ the uncertainty in q is mainly governed by the wavelength spread (Figure 2). At the position of n^{th} Bragg peak, equation (4) becomes:

$$\Delta q_b^{n\,2} = n^2 \Delta q_b{}^2(l) + \Delta q_b^{n\,2}(q) \qquad \textbf{(7)}$$

- We consider first that the crystalline structure factor is ideal and gives delta function at the positions q_n equal to q_b, $2q_b$, …, nq_b, n being an integer. The structure factor smeared by the resolution function may be developed as a sum of gaussian functions of maxima at q_b, $2q_b$, …, nq_b:

$$S_{cristal}(q) = \sum_N A_n R_n\left(q, q_n, \Delta q_b^n\right) \text{ with} \qquad \textbf{(8)}$$

$$R_n\left(q, q_n, \Delta q_b^n\right) = \frac{1}{n\Delta q_b^n \sqrt{2p}} \exp\left(-\frac{(q-nq_b)^2}{2\left(\Delta q_b^n\right)^2}\right), \text{ the resolution function}$$

A_n is a scaling intensity factor.

We call $\left(\Delta q_b^n\right)_{\exp}$, the characteristic width (see appendix) of the experimental n^{th} Bragg peak assuming a gaussian geometry. The wavelength resolution is directly deduced from the data by:

$$\left(\frac{\Delta l}{l}\right) = \frac{2\sqrt{2\ln 2}}{nq_b} \sqrt{\left[\left(\Delta q_b^n\right)_{\exp}\right]^2 - \left[\Delta q_b^n(q)\right]^2} \qquad \textbf{(9)}$$

- In a more realistic case, the Bragg peaks have a finite size and a gaussian shape described by $P_n(q,nq_b,Dq_c)$. The real structure factor is the sum of:

$$S_{cristal}(q) = \sum_N A_n S_n(q_n) \text{ with} \qquad \textbf{(10)}$$

$$S_n(q, nq_b, \Delta q_c) = \frac{1}{\Delta q_c \sqrt{2p}} \exp\left(-\frac{(q - nq_b)^2}{2(\Delta q_c)^2} \right)$$

Where Dq_c is related to the variation around the nominate periodicity:

$$\Delta q_c = \frac{q_b^2 \Delta d_b}{2p} \qquad \textbf{(11)}$$

Dd_b is the variation of period in the real space around d_b, the average period ($d_b = 2p/q_b$).

After smearing by the resolution function $R(q', q, \Delta q_b^n)$, $S_{cristal}(q)$ becomes:

$$S_{cristal}(q) = \sum_N A_n \int_{q-a}^{q+a} S_n(q', q_n, \Delta q_c) R(q', q, \Delta q_b^n) \qquad \textbf{(12)}$$

$$\text{with } R(q', q, \Delta q_b^n) = \frac{1}{n\Delta q_b^n \sqrt{2p}} \exp\left(-\frac{(q'-q)^2}{2(\Delta q_b^n)^2} \right)$$

$$S_{cristal}(q) = \sum_N \frac{1}{2pn\Delta q_b^n \Delta q_c} \int_{q'-a}^{q'+a} \exp\left(-\frac{(q'-q)^2}{2(\Delta q_b^n)^2} \right) \exp\left(-\frac{(q'-nq_b)^2}{2(\Delta q_c)^2} \right) dq'$$

The smearing of two gaussian functions is also a gaussian function of characteristic width $(\Delta q_b^n)_{\exp}$, but there is no simple analytical expression to link it with Δq_b^n and Δq_c. The calculation has to be done numerically. We developed a Fortran program with input parameters Dq_c and $(\Delta q_b^n)_{\exp}$ (the characteristic width of the experimental nth Bragg peak). The program increases (Δq_b^n) by step of 10^{-4} from an initial value of 2×10^{-4} Å^{-1} and calculates the reduced chi-squared c^2 between the data obtained by convolution (12) and the gaussian of width $(\Delta q_b^n)_{\exp}$. It selects the parameter corresponding to the smallest c^2.

$$c^2 = \sum_{nq} \left[\frac{S(q) - G(q, \Delta q_b^n)}{dS(q)} \right]^2 \Big/ (nq - 1) \qquad \textbf{(13)}$$

Where nq is the number of points of calculation.

The wavelength spread is then deduced from (Δq_b^n) with (9).

This experiment has been done on D22 (ILL) with silver behenate. Silver behenate was purchased by Johnson Matthey chemicals and used without further treatment, but kept in a dry dark place. Three wavelengths 6, 8 and 10 Å have been used. The collimation distances C were varied from 17.6 m to 2.8 m to show broadening of the Bragg peak width due to divergence of the direct beam. The sample to detector distance was fixed at 2 m, with a 390 mm detector offset, to cover the largest possible q-range. For the two smallest collimation distances, an attenuator was placed in the

beam to avoid detector damage due to the high count rates in the Bragg peaks. In these experimental conditions, three Bragg peaks are visible for λ=6 and 8 Å, two for λ=10 Å. After a radial averaging, the data were divided by a water spectra measured in the same experimental conditions in order to correct the detector geometry.

The Bragg peaks are fitted with a gaussian function. The half widths $\left(\Delta_b^n\right)_{\exp}$ are summarized in Table 1. The shapes and sizes of the direct beam are shown in Figure 11 for λ=6 Å. An example of spectra obtained with λ =6 Å and C=14.4 m where three Bragg peaks are visible is presented in Figure 6.

Firstly, we have assumed that Bragg peaks from the Ag-Behenate were infinitely sharp (Δq_c=0). We note here that the width of the experimental Bragg peaks does not vary for *Dq* smaller or equal to 10^{-3} rad. From (9), we deduce an average value for the wavelength distribution of $\Delta\lambda/\lambda$ =0.134 for the 1st order Bragg peak, $\Delta\lambda/\lambda$=0.122 for the 2nd order Bragg peak. The values found are slightly too high, in comparison with that obtained with time of flight measurement. The overestimate of $\Delta\lambda/\lambda$ may be due to the hypothesis Δq_c =0.

Consequently, the silver behenate was also studied on the x-ray beam line D2AM at the ESRF so that the wavelength spread ($\Delta\lambda/\lambda = 10^{-4}$) is negligible. It was measured for 10 s at 15.02 keV and recorded on a CCD camera, to get a good spatial resolution. *Dq(0)* (direct beam) was 0.0019 $Å^{-1}$ (*Dq* =1.18x10^{-4} rad) with the configuration used and the characteristic width of the first order Bragg peak is $\left(\Delta q_b^1\right)_{\exp}$ = 0.004 $Å^{-1}$. From (12) and the method described above, we deduced Δq_c =0.0035 $Å^{-1}$ (Δq_c^2=1.22x10^{-5} $Å^{-2}$). Δq_c is thus not negligible; it is of the same order as $Dq_n^2(q)$ (see Table 1). The wavelength spreads have been calculated again with (12). The values of $\left(\Delta q_b^n\right)$ corrected from the silver behenate period spread Δq_c are given in the Table 2. $\Delta\lambda/\lambda$ is deduced with (9). The average value for $\Delta\lambda/\lambda$ is now 0.109 (±0.007) for the 1rst order Bragg peak and 0.113 (±0.004) for the 2nd order Bragg peak, in good agreement with the 10% determined by time of flight.

The values of $\Delta\lambda/\lambda$ obtained with time of flight experiment and with the method presented here are in good agreement. From an experimental point of view, our measurement is easy to do in comparison with a time of flight experiment that requires adapting the instrument. However, the data treatment needs further development and a good knowledge of the sample is essential.

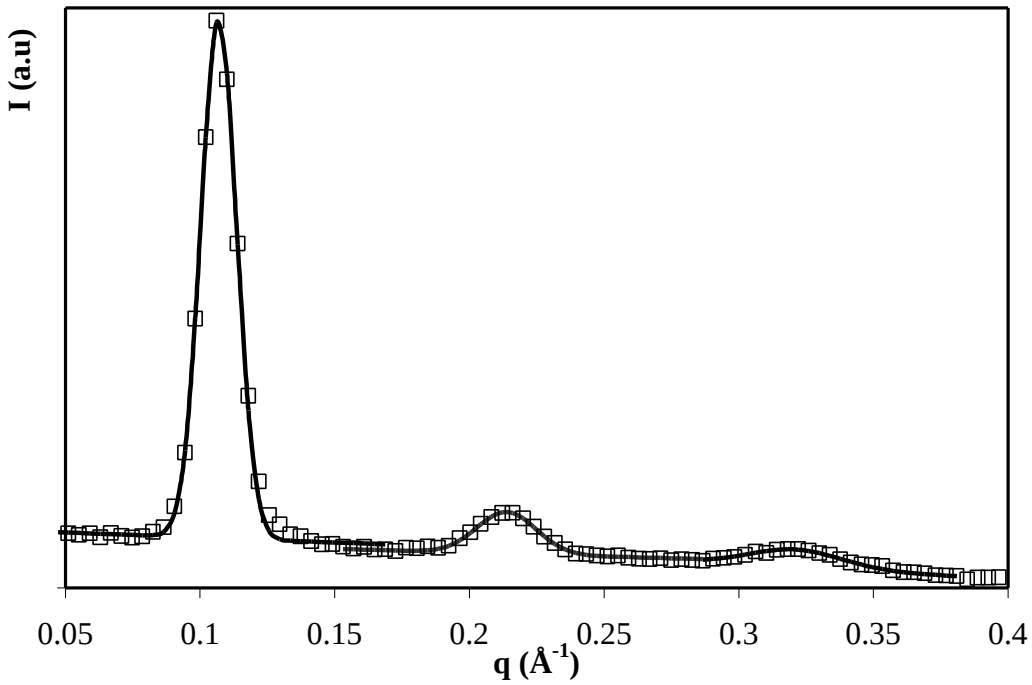

Figure 6: Example of SANS spectra of silver behenate obtained for λ=6 Å and Collimation=14.4 m. Squares are the experimental points, full lines are the best fits obtained with gaussian functions.

Polydispersity

Most colloidal suspensions are composed of polydisperse objects. The form factor of monodisperse particles $F^2(q,r_0)$ (1) is smeared with the size distribution function $G(r_o,r,x)$, where x is the parameter characterizing the width of the distribution:

$$I_{poly}(q,r_o) = \int_0^\infty K_c G(r_o,r,x) F^2(q,r_o) dr \qquad \textbf{(14)}$$

Gaussian, log-normal functions or Schultz distribution are often used to represent the size spread, around an average value r_o. The normalized expressions ($\int_0^\infty G(r)dr = 1$) are given here; their shapes and principal properties compared in Figure 7.

- The gaussian function is:

$$G_G(r_o,r,\Delta r_o) = \frac{1}{\Delta r_o \sqrt{2p}} \exp\left(-\frac{(r-r_o)^2}{2\Delta r_o{}^2}\right) \qquad \textbf{(15)}$$

where Dr_o is the half-width of the gaussian function for $G_G(r_o, r_0 + \Delta r_0) = G(r_o)\exp(-1/2) = 0.606$. The gaussian function is symmetric about its maximum r_o.

- The log-normal distribution is equal to:

$$G_{LN}(r_o, r, s_o) = \frac{1}{r s_o \sqrt{2p}} \exp\left(-\frac{1}{2 s_o^2} \left(\ln \frac{r_o}{r} \right)^2 \right) \quad \textbf{(16)}$$

σ_0 is the standard mean deviation, related to the half width by $\Delta r_0 = \sigma_0 r_0$. The maximum of the function is found for $r = r_o \exp\left(-s_o^2\right)$.

- The Schultz distribution is:

$$G_S(r_o, r, Z) = \left(\frac{Z+1}{r_o} \right)^{Z+1} \exp\left(-\frac{Z+1}{r_o} r \right) / \Gamma(Z+1) \text{ with} \quad \textbf{(17)}$$

$$\Gamma(Z) = \int e^{-t} t^{Z-1} dt \text{, the gamma function}$$

The root mean square deviation from the mean is $s = r_o / (Z+1)^{1/2}$. The maximum of the curve is found at $R = Z r_o / (Z+1)$

The three functions are plotted in Figure 7. r_o is fixed at 200 Å. For the log-normal and the Schultz functions, the maximum of the curves are slightly smaller than r_o. The half-widths at $G(r_o)\exp(-1/2)$ are related by:

$$\Delta r_o(gaussian) = s_o r_o(\log\text{-}normal) = r_o / (Z+1)^{1/2} (Schultz) \quad \textbf{(18)}$$

Finally, these three expressions yield very similar numerical values (Figure 7) and it is certainly not possible to distinguish them by a SANS experiment.

In the following, we will use a log-normal law to illustrate the effects of polydispersity.

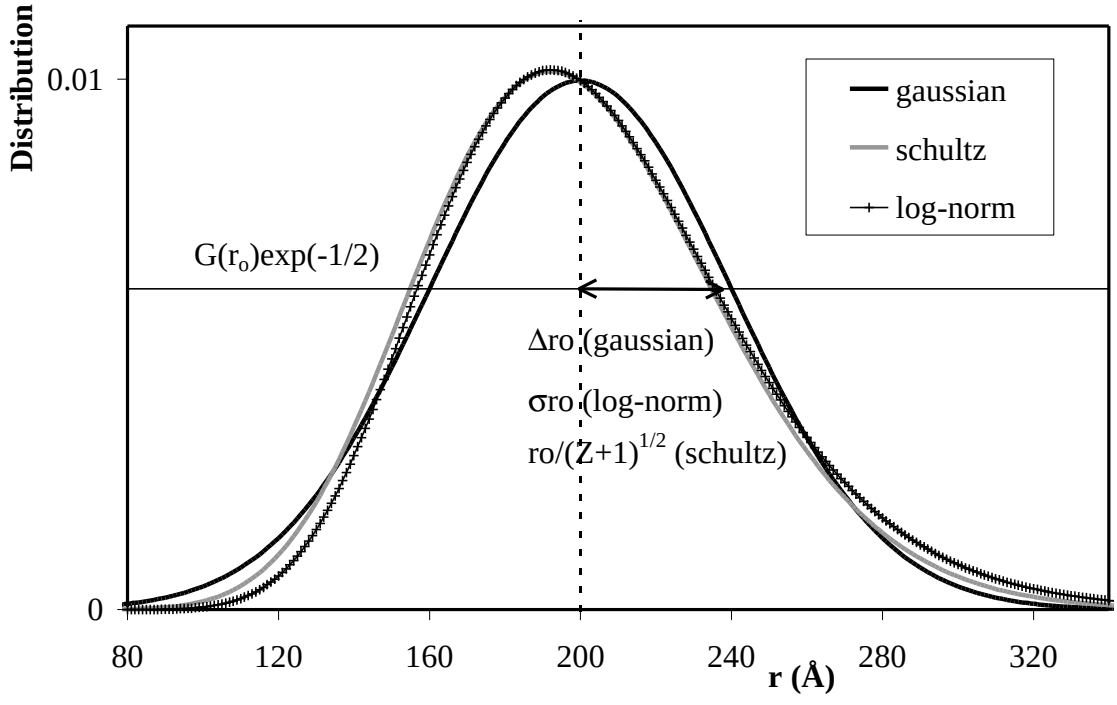

Figure 7: Comparison of the 3 size distribution laws. r_o=200 Å; Dr_o =40 Å (gaussian); s_o=0.2 (log-normal) and Z=90 (Schultz).

The effect of polydispersity on the form factor of a spherical shell of inner radius of 200 Å is illustrated in Figure 8. It is clearly visible for σ_0 > 10%. The oscillations vanish and the minimum of the first oscillation is shifted to higher q-values.

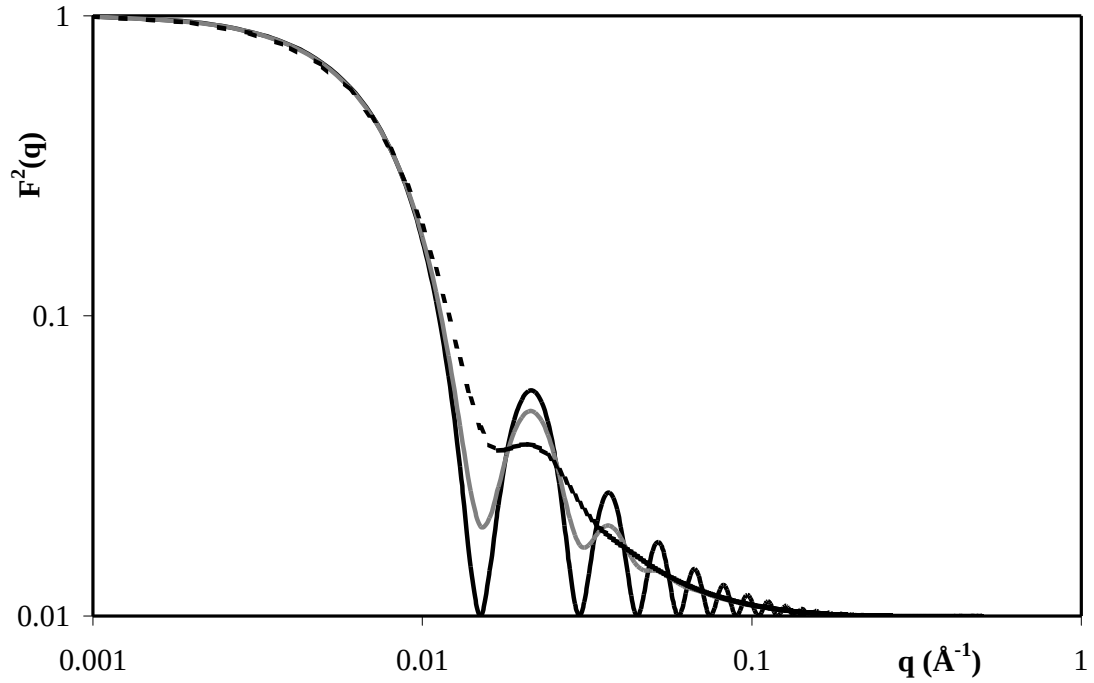

Figure 8: Effect of the polydispersity on the ideal scattering of a monodisperse spherical shell, r_0=200 Å. (▬) s_0=0; (▬) s_0=10%; (▪▪▪▪) s_0=20%.

Instrumental resolution and polydispersity

If one compares Figure 5 and Figure 8, the effect of polydispersity or wavelength resolution are very similar. Indeed, mathematically, the smearing equations (6) and (14) are similar. An experimental curve results from the smearing of the ideal intensity both by the resolution and the polydispersity functions:

$$I_{\exp}(q_o, r_o) = \int_0^{\infty} R(q - q') \left[\int_0^{\infty} K_c G(r_o) F^2(r_o, q) dr_o \right] dq' \qquad \textbf{(19)}$$

$$I_{\exp}(q_o, r_o) = \int_0^{\infty} R(q_o, q') \left[\int_0^{\infty} K_c G(r_o, r) F^2(r_o, q) dr \right] dq'$$

As q and r_0 are independent variables, (19) is also equal to:

$$I_{\exp}(q_o, r_o) = \int_{R=0}^{R\to\infty} \int_{q\to-\infty}^{q\to+\infty} K_c R(q_o, q) G(r_o, r) F^2(r_o, q_o, r, q) dr dq \qquad \textbf{(20)}$$

Remark: Taking a Gaussian law for the polydispersity, the total resolution function is symmetrical according the variables q and r. Thus, the smearing effects due to Dr_o or Dq_o may be equivalent.

It is interesting now to compare the two smearing influences. We consider $\Delta\lambda/\lambda$=10%, and a spherical shell of inner radius r_0=200 Å, outer one 220 Å and polydispersity σ_0=0.2 (r_0=200 ± 40 Å). These values are typically found with a dilute sample of AOT, an anionic surfactant (Fontell, 1973) in a dilute salt suspension. The calculated intensity is shown in Figure 9. Equivalent spectra are obtained either by fixing $\Delta\lambda/\lambda$ at 42% or the radius polydispersity at 0.22 (r_0=200 ± 44 Å). This example shows clearly that the smooth of the pattern is mainly due to the sample characteristics and not to the spectrometer resolution.

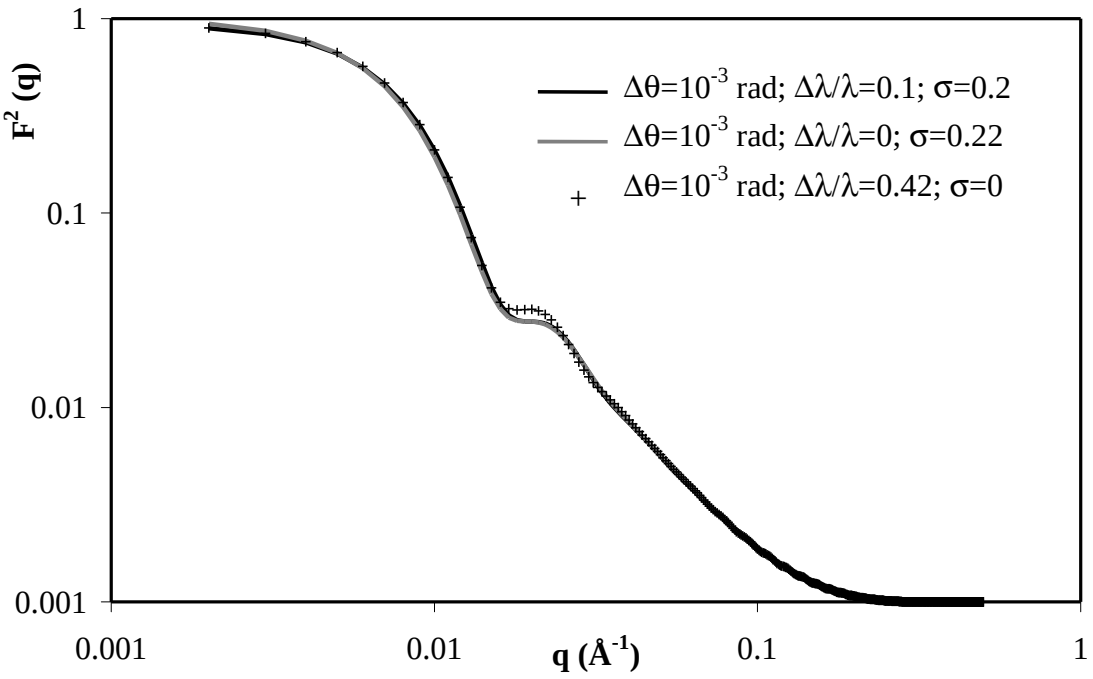

Figure 9: Comparison of the effect of polydispersity and wavelength resolution on the shell form factor. l**=6 Å,** Dq**=10^{-3} rad. A realistic spectra obtained with** Dl/l**=10% and** s**=0.2 is equivalent to a spectra obtained with** Dl/l**=0% and** s**=0.22 or** Dl/l**=42% and** s**=0.**

Conclusion

The contribution of the instrumental resolution to the scattering pattern is a general question. This knowledge is crucial for the data analysis because instrumental resolution and sample polydispersity have similar smearing effects on the SANS data. Smoothing of the form factor oscillations, broadening of Bragg peaks or of the maxima are observed. Plotting I(q) versus q in a log-log representation may show a decrease of the initial slope, due to a smearing by a large direct beam may also be present (Né *et al.*, 2000). As shown with simulation, 20% is the limiting value above

which the smearing effect by the wavelength becomes drastic and yields to a real change in the scattered pattern.

For the spectrometer D22 (ILL), the conclusions are the following. At low q ($< 5x10^{-2}$ $Å^{-1}$), the smearing is dominated by the size and divergence of the direct beam. At large q ($>10^{-1}$ $Å^{-1}$), the wavelength spread dominates the smearing and enlargement of Bragg peaks (for example) may be observed. The 10% wavelength resolution is not a limiting factor to measuring possible form factor oscillations. The beam divergence does not affect the shape of the Bragg peaks measured at large q (> 0.1 $Å^{-1}$) as long as the angular divergence Dq is smaller than 10^{-3} rad as demonstrated with the silver behenate experiments when varying the collimation distance. The choice of collimation is a compromise between the flux and the resolution that has to be considered for each experiment.

Acknowledgements: I am very grateful to Ron Ghosh (ILL) for its careful reading and commentaries discussion. I wish to thank R. May for all of his help and discussions during the test times and the manuscript writing. I thank C. Rochas (CNRS, Grenoble) for the measurement of Silver Behenate on the beam line D2AM at the ESRF.

Appendix: Definition of Dq and Dl/l; comparison between triangle and gaussian functions

In the entire text gaussian functions are used to describe the wavelength and the angular distribution. We define here where the widths are taken. Indeed, the $\Delta\lambda/\lambda$ usually given is the FWHM and has to be replaced by Dx_0, the width parameter in the gaussian equation.

We recall that a gaussian function centered on x_o of half width Δx_0 at the value $G(x, x_0, \Delta x_0) = \frac{1}{\sqrt{2p}\,\Delta x_0}\exp(-1/2)$ is given by:

$$G(x, x_0, \Delta x_0) = \frac{1}{\sqrt{2p}\,\Delta x_0}\exp\left(-\frac{(x-x_0)^2}{2\Delta x_0{}^2}\right) \quad \textbf{(21)}$$

The FWHM of a gaussian is:

$$FWHM = 2\Delta x_0\sqrt{2\ln 2} \quad \textbf{(22)}$$

Wavelength distribution

The wavelength distribution is ideally triangular but experiments show that gaussian fits gives reasonable results and improve the numerical treatment (Pedersen *et al.*, 1990). $\Delta\lambda/\lambda$ is deduced from the FWHM of the triangular function. It is usually between 5% and 20% with a neutron velocity selector, a value determined by time of flight measurements. Gaussian and triangular function are compared in Figure 10.

A triangular function of unit area, centered on λ_o of FWHM $\lambda_o(\Delta\lambda/\lambda)$ is given by:

$$T(l) = \frac{1}{[l_0(\Delta l/l)]^2}\,l + \frac{l_0(1-(\Delta l/l))}{[l_0(\Delta l/l)]^2};\; l \le l_0 \quad \textbf{(23)}$$

$$T(l) = \frac{-1}{[l_0(\Delta l/l)]^2}\,l + \frac{l_0(1+(\Delta l/l))}{[l_0(\Delta l/l)]^2};\; l \ge l_0$$

Now, for calculation, we use a gaussian function where the relevant parameter is σ_λ, the half width at the value $\frac{1}{\sqrt{2p}\,s_l}\exp(-1/2)$.

We replace the triangular function by a gaussian one with the same FWHM. From (22), one deduces:

$$s_{\lambda} = \frac{\lambda_0 (\Delta\lambda/\lambda)}{2\sqrt{2\ln 2}} \qquad \textbf{(24)}$$

Thus, the relative wavelength spread introduces in (1) is:

$$(d\lambda/\lambda) = \frac{(\Delta\lambda/\lambda)}{2\sqrt{2\ln 2}} \qquad \textbf{(25)}$$

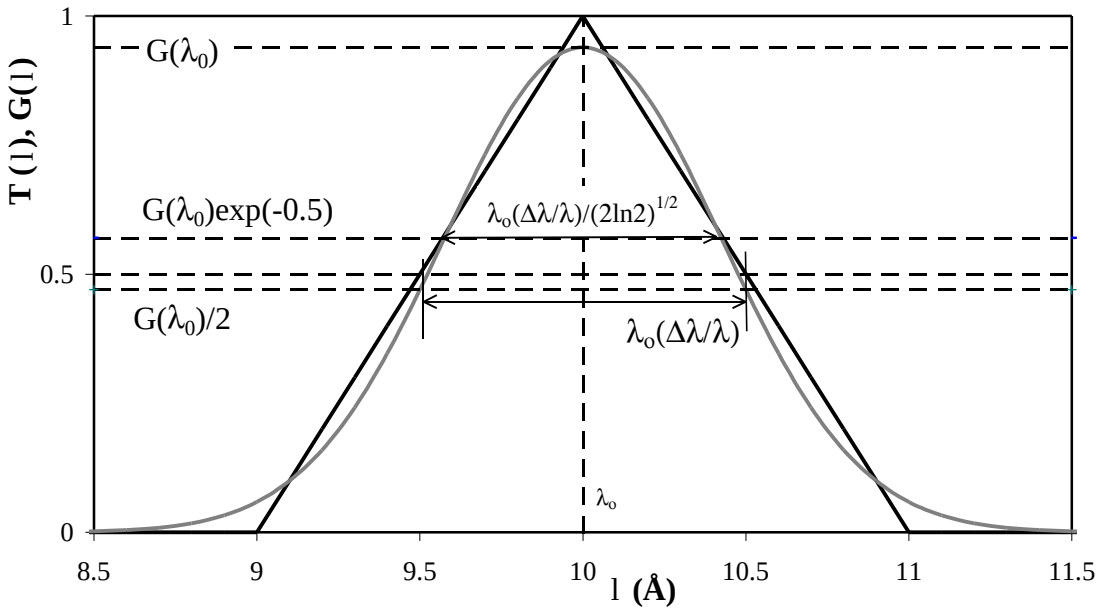

Figure 10: Comparison between triangular and gaussian functions with the same areas used to represent the wavelength distribution.

Angular distribution

The angular distribution *Dq* is deduced from the width of the direct beam. On q=0, θ= 0 and (3) is reduced to:

$$\Delta q(0) = \frac{4p}{\lambda}\Delta q \qquad \textbf{(26)}$$

On D22, the measurements show that reasonable fits are obtained with a gaussian function, even if deviation is observed in the tails. In these conditions *Dq(0)* is equivalent to Dx_0 in (21) and one easily deduce *Dq* with (26).

Dq can also be calculated with the geometry of the instrument. We have seen in the introduction that the beam size on the detector was $S_d = S\,D/C$. The direct beam divergence is:

$$\Delta q = S_d / C \qquad \textbf{(27)}$$

Example of experimental direct beam shapes for λ=6 Å and various collimation distances C are presented in Figure 11.

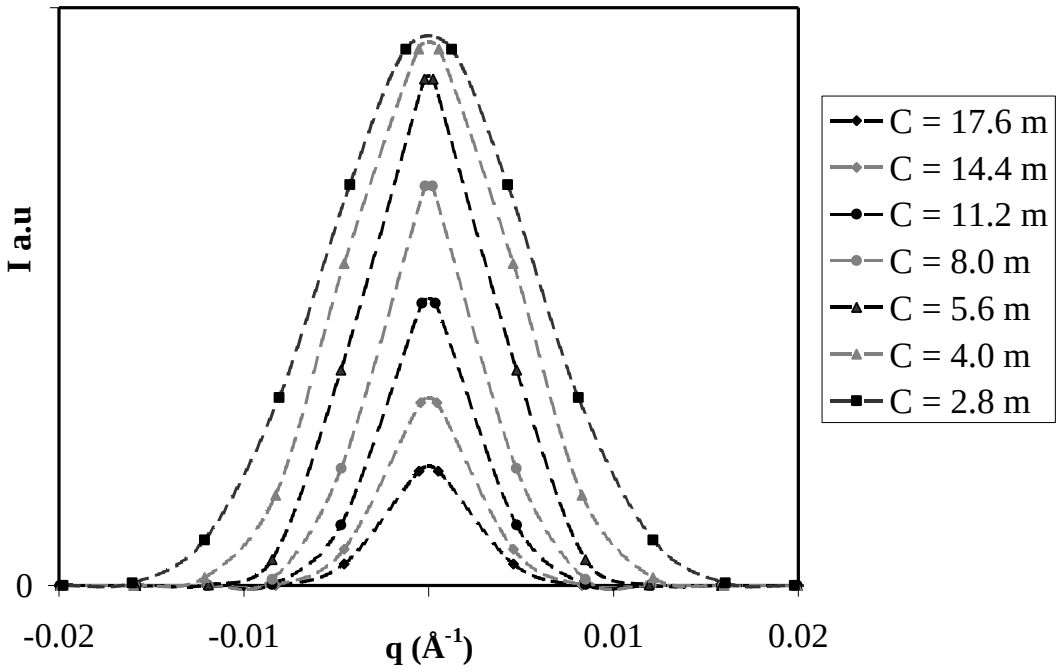

Figure 11: Shape and size of the direct beam of D22 at λ=6 Å for the different possible collimation distances. Dotted lines are a guide for the eyes.

Tables

l = 6 Å							
Coll.(m)	17.6	14.4	11.2	8.0	5.6	4.0	2.8
Dq (rad)	$1.109\ 10^{-3}$	$1.14\ 10^{-3}$	$1.18\ 10^{-3}$	$1.48\ 10^{-3}$	$1.76\ 10^{-3}$	$2.10\ 10^{-3}$	$2.57\ 10^{-3}$
1rst Bragg peak							
$\left(\Delta q_b^1\right)_{\exp}$ (Å^{-1})	0.0066	0.0066	0.0066	0.0069	0.0072	0.0071	0.0078
$Dq_1^2(q)$	$5.20\ 10^{-6}$	$5.68\ 10^{-6}$	$6.09\ 10^{-6}$	$9.58\ 10^{-6}$	$1.35\ 10^{-5}$	$1.93\ 10^{-5}$	$2.89\ 10^{-5}$
Dl/l **(q_b)**	**0.135**	**0.134**	**0.134**	**0.135**	**0.135**	**0.130**	**0.134**
2nd Bragg peak							
$\left(\Delta q_b^2\right)_{\exp}$ (Å^{-1})	0.011	0.011	0.011	0.0112	0.0115	- *	- *
$Dq_2^2(q)$	$5.09\ 10^{-6}$	$5.56\ 10^{-6}$	$5.96\ 10^{-6}$	$9.38\ 10^{-6}$	$1.33\ 10^{-5}$	$1.89\ 10^{-5}$	$2.83\ 10^{-5}$
Dl/l **($2q_b$)**	**0.118**	**0.117**	**0.117**	**0.118**	**0.119**	- *	- *
3rd Bragg peak							
$\left(\Delta q_b^3\right)_{\exp}$ (Å^{-1})	0.018	0.017	0.0165	0.0165	- *	- *	- *
$Dq_3^2(q)$	$5.08\ 10^{-6}$	$5.56\ 10^{-6}$	$5.96\ 10^{-6}$	$9.38\ 10^{-6}$	$1.33\ 10^{-5}$	$1.89\ 10^{-5}$	$2.83\ 10^{-5}$
Dl/l **($3q_b$)**	**0.130**	**0.123**	**0.119**	**0.118**	- *	- *	- *

l = 8 Å							
Coll.(m)	17.6	14.4	11.2	8.0	5.6	4.0	2.8
Dq **(rad)**	$1.11\ 10^{-3}$	1.2110^{-3}	$1.27\ 10^{-3}$	$1.34\ 10^{-3}$	$1.78\ 10^{-3}$	$2.39\ 10^{-3}$	$3.18\ 10^{-3}$
1rst Bragg peak							
$\left(\Delta q_b^1\right)_{\exp}$ (Å^{-1})	0.0063	0.0063	0.0063	0.0063	0.0067	0.0068	0.0078
$Dq_1^2(q)$	$1.72\ 10^{-6}$	$2.02\ 10^{-6}$	$2.24\ 10^{-6}$	$2.46\ 10^{-6}$	$4.41\ 10^{-6}$	$7.87\ 10^{-6}$	$1.39\ 10^{-5}$
Dl/l **(q_b)**	**0.132**	**0.131**	**0.131**	**0.130**	**0.131**	**0.124**	**0.126**
2nd Bragg peak							
$\left(\Delta q_b^2\right)_{\exp}$ (Å^{-1})	0.011	0.011	0.011	0.011	0.0115	0.012	0.012
$Dq_2^2(q)$	$5.20\ 10^{-6}$	$5.68\ 10^{-6}$	$6.09\ 10^{-6}$	$9.58\ 10^{-6}$	$1.35\ 10^{-5}$	$1.93\ 10^{-5}$	$2.89\ 10^{-5}$
Dl/l **($2q_b$)**	**0.119**	**0.118**	**0.118**	**0.118**	**0.122**	**0.125**	**0.126**
3rd Bragg peak							
$\left(\Delta q_b^3\right)_{\exp}$ (Å^{-1})	0.017	0.017	0.017	- *	- *	- *	- *
$Dq_3^2(q)$	$1.72\ 10^{-6}$	$2.03\ 10^{-6}$	$2.25\ 10^{-6}$	- *	- *	- *	- *
Dl/l **($3q_b$)**	**0.116**	**0.116**	**0.116**	- *	- *	- *	- *

l =10 Å						
Coll.(m)	17.6	14.4	11.2	8.0	5.6	4.0
Dq **(rad)**	$6.70\ 10^{-4}$	$7.60\ 10^{-4}$	$9.50\ 10^{-4}$	$1.00\ 10^{-3}$	$1.05\ 10^{-3}$	$1.40\ 10^{-3}$
1rst Bragg peak						
$\left(\Delta q_b^1\right)_{\exp}$ (Å^{-1})	0.0063	0.0063	0.0063	0.0064	0.0066	0.0068
$Dq_1^2(q)$	$7.04\ 10^{-7}$	$9.05\ 10^{-7}$	$1.41\ 10^{-6}$	$1.90\ 10^{-6}$	$1.97\ 10^{-6}$	$3.21\ 10^{-6}$
Dl/l **(q_b)**	**0.134**	**0.133**	**0.131**	**0.131**	**0.132**	**0.131**
2nd Bragg peak						
$\left(\Delta q_b^2\right)_{\exp}$ (Å^{-1})	0.011	0.011	0.011	0.011	0.011	- *
$Dq_2^2(q)$	$7.09\ 10^{-7}$	$9.12\ 10^{-7}$	$1.43\ 10^{-6}$	$1.91\ 10^{-6}$	$1.98\ 10^{-6}$	- *
Dl/l **($2q_b$)**	**0.119**	**0.119**	**0.118**	**0.118**	**0.118**	- *

Table 1: Determination of $\Delta\lambda/l$ according to wavelength and direct beam width. $\left(\Delta q_b^n\right)_{\exp}$ is the half width of the experimental bragg peaks. We suppose here Dq_c=0.

*** Bad statistic on the Bragg peak for a good fit.**

l = **6 Å**							
Coll.(m)	17.6	14.4	11.2	8.0	5.6	4.0	2.8
Dq (rad)	$1.109\ 10^{-3}$	$1.14\ 10^{-3}$	$1.18\ 10^{-3}$	$1.48\ 10^{-3}$	$1.76\ 10^{-3}$	$2.10\ 10^{-3}$	$2.57\ 10^{-3}$
1rst Bragg peak							
$\left(\Delta q_b^1\right)_{cor}$ **(Å^{-1})**	0.0057	0.0057	0.0057	0.0060	0.0064	0.0063	0.0071
$Dq_1^2(q)$	$5.20\ 10^{-6}$	$5.68\ 10^{-6}$	$6.09\ 10^{-6}$	$9.58\ 10^{-6}$	$1.35\ 10^{-5}$	$1.93\ 10^{-5}$	$2.89\ 10^{-5}$
Dl/l **(q_b)**	**0.114**	**0.113**	**0.112**	**0.112**	**0.114**	**0.099**	**0.101**
2nd Bragg peak							
$\left(\Delta q_b^2\right)_{cor}$ **(Å^{-1})**	0.0105	0.0105	0.0105	0.0107	0.0111	- *	- *
$Dq_2^2(q)$	$5.09\ 10^{-6}$	$5.56\ 10^{-6}$	$5.96\ 10^{-6}$	$9.38\ 10^{-6}$	$1.33\ 10^{-5}$	$1.89\ 10^{-5}$	$2.83\ 10^{-5}$
Dl/l **($2q_b$)**	**0.112**	**0.112**	**0.112**	**0.112**	**0.115**	- *	- *
3rd Bragg peak							
$\left(\Delta q_b^3\right)_{cor}$ **(Å^{-1})**	0.0178	0.0162	0.0162	0.0162	- *	- *	- *
$Dq_3^2(q)$	$5.08\ 10^{-6}$	$5.56\ 10^{-6}$	$5.96\ 10^{-6}$	$9.38\ 10^{-6}$	$1.33\ 10^{-5}$	$1.89\ 10^{-5}$	$2.83\ 10^{-5}$
Dl/l **($3q_b$)**	**0.118**	**0.117**	**0.117**	**0.116**	- *	- *	- *

l = **8 Å**							
Coll.(m)	17.6	14.4	11.2	8.0	5.6	4.0	2.8
Dq **(rad)**	$1.11\ 10^{-3}$	1.2110^{-3}	$1.27\ 10^{-3}$	$1.34\ 10^{-3}$	$1.78\ 10^{-3}$	$2.39\ 10^{-3}$	$3.18\ 10^{-3}$
1rst Bragg peak							
$\left(\Delta q_b^1\right)_{cor}$ **(Å^{-1})**	0.0053	0.0053	0.0053	0.0053	0.0058	0.0059	0.0071
$Dq_1^2(q)$	$1.72\ 10^{-6}$	$2.02\ 10^{-6}$	$2.24\ 10^{-6}$	$2.46\ 10^{-6}$	$4.41\ 10^{-6}$	$7.87\ 10^{-6}$	$1.39\ 10^{-5}$
Dl/l **(q_b)**	**0.109**	**0.108**	**0.107**	**0.106**	**0.111**	**0.100**	**0.111**
2nd Bragg peak							
$\left(\Delta q_b^2\right)_{cor}$ **(Å^{-1})**	0.0105	0.0105	0.0105	0.0105	0.0111	0.0116	0.0116
$Dq_2^2(q)$	$5.20\ 10^{-6}$	$5.68\ 10^{-6}$	$6.09\ 10^{-6}$	$9.58\ 10^{-6}$	$1.35\ 10^{-5}$	$1.93\ 10^{-5}$	$2.89\ 10^{-5}$
Dl/l **($2q_b$)**	**0.113**	**0.113**	**0.113**	**0.113**	**0.117**	**0.120**	**0.114**
3rd Bragg peak							
$\left(\Delta q_b^3\right)_{cor}$ **(Å^{-1})**	0.0157	0.0157	0.0157	- *	- *	- *	- *
$Dq_3^2(q)$	$1.72\ 10^{-6}$	$2.03\ 10^{-6}$	$2.25\ 10^{-6}$	- *	- *	- *	- *
Dl/l **($3q_b$)**	**0.114**	**0.114**	**0.114**	- *	- *	- *	- *

l = **10 Å**						
Coll.(m)	17.6	14.4	11.2	8.0	5.6	4.0
Dq **(rad)**	$6.70\ 10^{-4}$	$7.60\ 10^{-4}$	$9.50\ 10^{-4}$	$1.00\ 10^{-3}$	$1.05\ 10^{-3}$	$1.40\ 10^{-3}$
1rst Bragg peak						
$\left(\Delta q_b^1\right)_{cor}$ **(Å^{-1}**	0.0053	0.0053	0.0053	0.0055	0.0057	0.0059
$Dq_1^2(q)$	$7.04\ 10^{-7}$	$9.05\ 10^{-7}$	$1.41\ 10^{-6}$	$1.90\ 10^{-6}$	$1.97\ 10^{-6}$	$3.21\ 10^{-6}$
Dl/l **(q_b)**	**0.112**	**0.111**	**0.107**	**0.109**	**0.114**	**0.111**
2nd Bragg peak						
$\left(\Delta q_b^2\right)_{cor}$ **(Å^{-1})**	0.0105	0.0105	0.0105	0.0105	0.0105	- *
$Dq_2^2(q)$	$7.09\ 10^{-7}$	$9.12\ 10^{-7}$	$1.43\ 10^{-6}$	$1.91\ 10^{-6}$	$1.98\ 10^{-6}$	- *
Dl/l **($2q_b$)**	**0.114**	**0.113**	**0.113**	**0.112**	**0.112**	- *

Table 2: Determination of $\Delta\lambda/l$ for various wavelengths and direct beam widths after correction of $\left(\Delta q_b^n\right)_{\exp}$ from the period variation of the silver behenate, Dq_c=0.004 Å^{-1}.

References

D22 manual http://www.ill.fr/YellowBook/D22/.

Debye, P. (1947). *J. Phys. Colloid Chem*. **51**, 18-32.

Fontell, K. (1973). *J. of Colloid and Interface Sc*. **44**, 156-164 and 318-329.

Fournet, G. (1951). *Bull. Soc. Fr. Minéral Crist*. **74**, 39-113.

Guinier, A. (1939). *Ann. Phys* **12**, 161-237.

Huang, T.C, Toraya, H., Blanton, T.N., Wu, Y. (1993). *J. Appl. Cryst*. **26**, 180-184.

Lord Rayleigh (1911). *Proc. Roy. Soc. London* Ser. A**, 84**, 25-38.

Mildner, D.F.R. (1990). *Nuclear Instruments and Methods in physics Research* A**290**, 259-262.

Né, F., Grillo, I., Taché, O., Zemb, Th. (2000). *J. Phys. IV* **10**, 103-413 and ref. inside.

Pedersen, J. S. (1997). *Adv. Colloid Interface Sci.* **70**, 171-210 and ref inside.

Pedersen, J.S, Posselt, D., Mortensen, K. (1990). *J. Appl. Cryst*. **23**, 321-333.

Schmatz, W., Springer, T., Schelten, J., Ibel, K. (1974). *J. Appl. Cryst*. **7**, 96-116.

Teixeira, J. (1988). *J. Appl. Cryst*. **21**, 781-785.

Wignall, G. D., Christen, D. K., Ramakrishnan, V. (1988) *J. Appl. Cryst*. **21**, 438-451.